Journal of Micromechanics and Microengineering

Active real-time electric field control of the e-jet in near-field electrospinning using an auxiliary electrode

OPEN ACCESS
IOP Publishing
Journal of Micromechanics and Microengineering
J. Micromech. Microeng. **31** (2021) 035001 (10pp)
https://doi.org/10.1088/1361-6439/abd3f4

Active real-time electric field control of the e-jet in near-field electrospinning using an auxiliary electrode

Anton Karlsson, Henrik Bergman and Stefan Johansson

Division of Microsystems Technology, Department of Materials Science, Uppsala University, Uppsala, Sweden

E-mail: anton.karlsson@angstrom.uu.se

Received 4 September 2020, revised 13 November 2020
Accepted for publication 15 December 2020
Published 20 January 2021

Abstract

Near-field electrospinning (NFES) is an additive manufacturing technique that allows for both high-resolution 3D structures and a wide variety of printed materials. Typically, a high electric field between a nozzle, the spinneret, and the substrate creates a μm-sized jet of a supplied liquid material. With mm distances between spinneret and sample, it is possible to have a fair control of the lateral placement of the deposited material. The placement is, however, distributed by various electrostatic phenomena, and this is one of the present challenges in developing NFES into a more versatile technique. In this paper, a higher degree of control in NFES placement was achieved through manipulation of the electric field direction, using an auxiliary steering electrode. The position of a polycaprolactone plastic jet was determined in real-time with a camera attached to a stereo microscope. The measured position was used to calculate an applied potential to the steering electrode to guide the plastic jet to the desired position. The placement accuracy was measured both at the substrate and during flight using the camera and microscope. The higher control was revealed through the deposition of plastic fibers in a pattern with decreasing separation, with and without the active steering electrode enabled. It is in the authors' opinion that the fabrication of dense structures could be possible with further refinement of the technique.

Keywords: near-field electrospinning, electrohydrodynamics, e-jet printing, fiber control, closed-loop control

(Some figures may appear in colour only in the online journal)

1. Introduction

Near-field electrospinning (NFES), also known as electrohydrodynamic 3D-printing, is a recently developed method for direct-writing of micro- and nanofibers, with the potential of creating detailed structures in areas such as microelectronics and microelectromechanical systems [1]. The technique allows for printing scaffold structures but not yet general solid 3D-structures. This work aims at evaluating the possibility to develop the NFES technique into a general additive manufacturing process, in analogy with the fused deposition modeling processes, by the use of an active electrostatic steering system.

In the NFES process, a high voltage is applied between a spinneret, that is supplying liquid materials, and a substrate. The distance between the spinneret and substrate is typically up to a few mm. The strong electric field forms a Taylor cone of the liquid material, and as the electrostatic forces overcome the surface tension, an electrohydrodynamic-jet (e-jet) of liquid material is continuously ejected towards the substrate. Two

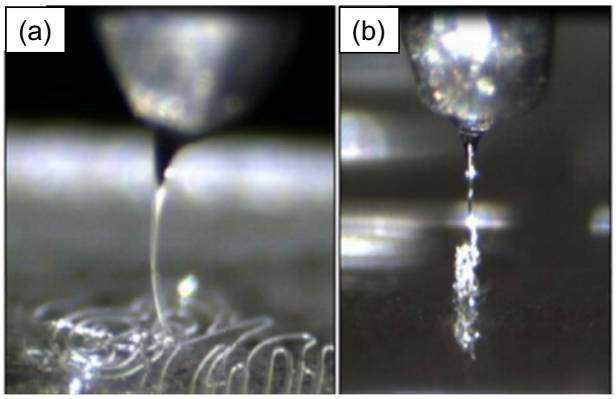

Figure 1. Stationary ejection of fiber for demonstration of the results of (a) high coulombic repulsion on a glass substrate, (b) low coulombic repulsion on a silicon substrate.

different liquid materials are typically used in near-field electrospinning; polymers dissolved in a solvent or, less commonly, molten polymers [2]. Melt-NFES, also known as melt electrowriting, was first introduced in 2011 as a method of creating 3D scaffolds and other structures [3]. Typically, melt-NFES produces larger diameter fibers than the solvent-based variant, but it is possible to reach sub-micrometer diameters using melt-NFES [4]. A commonly encountered problem of NFES is the charge effects of previously deposited material when printing on non-conductive substrates [5]. Even so, high-resolution 2D- and 3D-structures with 30 μm separation between plastic lines on a glass substrate are possible using melt-NFES, using a very short spinneret to substrate distance of 170 μm [6]. The deposited material forms both repulsive and attractive interactions with the polymer jet [5]. Using a substrate that dissipates the charges quickly, such as paper [7], the effect of Coulombic repulsion is decreased. Humidity in the air affects the adsorption of water on surfaces forming OH^- and H^+, which increases the surface conductivity of otherwise insulating substrates [8]. Due to the low radius of printed fiber on top of the otherwise flat substrate, the electric field gradient will be strongest at this sharp edge [5]. This creates a force with the opposite effect to the Coulombic repulsion, attracting the e-jet towards already deposited material on the substrate, and can cause stacking of fibers [5]. Figure 1 shows a demonstration of cases where the forces on the plastic jet are affected by high Coulombic repulsion, figure 1(a), and low Coulombic repulsion, figure 1(b). The fiber spreads out on the glass substrate in figure 1(a), and forms a pillar structure on a silicon substrate in figure 1(b). The electrostatic forces on the e-jet due to Coulombic repulsion and substrate shape, e.g. sharp edges of deposited fibers, typically prevent the e-jet from being printed in a straight line from the spinneret, orthogonally to the substrate, and the forces are increasing in magnitude as the distance between the e-jet and the previously printed structure decreases [5]. To the authors' knowledge, no dense 2D or 3D structures with material reliably deposited side-by-side, forming filled shapes, has been achieved using NFES to date.

Various methods have been shown to be able to increase the writing resolution of NFES and the more common far-field electrospinning (FFES): stretching and trailing the e-jet during NFES makes the deposited fibers more linear [9], allowing denser linear structures, but decreases control in patterns with corners or curves [10, 11]. Special NFES spinnerets that include a laminar flow of a sheath gas can constrain the e-jet [11–13]. The electric field in FFES can be focused into a controlled field through the use of electrostatic lenses and extractors [14–18], a sharp pin electrode beneath the substrate [19], or with a cylindrical side-wall electrode [20, 21], narrowing the printing area. A pre-defined printing pattern on a substrate can make it possible to build walls with ordered directions rather than the characteristic random orientation of the fiber using FFES [22]. Auxiliary electrodes have been used to steer electrospun fibers in FFES [23–25], and have also been used with solution-based NFES to produce wavy lines, via an alternating voltage being applied to the electrodes [26]. An auxiliary electrode has previously shown that the accuracy of NFES in corners can be increased [27]. In this work, an active steering system is added to a melt-NFES setup to increase the printing resolution. The added system dynamically affects the direction of the electric field by controlling the potential of an auxiliary electrode, steering the e-jet into the desired position. The input to the closed-loop control algorithm is the e-jet position, as measured through a camera at a fixed distance above the substrate surface. Melt-NFES is used in this work and the experimental parameters were selected to achieve a fiber with a diameter of around 10 μm, since such a wide melt polymer-jet is easier to identify with the camera. The viscosity of the polymer-jet in combination with the chosen width also results in lateral movements slow enough to be compatible with the present refresh rates of the algorithm. In this work, the effect of using an auxiliary steering electrode on the deposition resolution of fibers is evaluated. To prevent fiber stretching from too fast movement (fiber trailing) or whipping due to too slow movement (axisymmetric instability), stage movement speed and applied potential to the substrate are matched in this work.

2. Material and methods

2.1. Printing setup

The printing setup used was previously developed in-house and contains an XYZ-stage powered by three PiezoMotor LEGS LT2010A piezoelectric motors, connected to PiezoMotor DMC-30 019 controllers and HeidenHain optical position sensors LIP 403 for positional feedback. The XYZ-stage provides approximately 25 mm $\times$ 25 mm $\times$ 10 mm range of movement. A substrate consisting of a glass slide (10 mm $\times$ 10 mm $\times$ 140 μm, Assistant Deckgläser) attached with conductive carbon tape on a scanning electron microscope (SEM) substrate holder was mounted in the XYZ-stage. For tests adding successive layers to form a 3D-structure, the glass substrate was replaced with a 10 mm $\times$ 10 mm piece of a silicon wafer (orientation (100) with a resistivity of 0.004–0.006 Ωcm). The printing head was a VWR 100 μl micro syringe mounted above the substrate, with the spinneret being the needle cut and ground into a truncated cone shape. This microsyringe was heated by a soldering iron (Weller WT1)

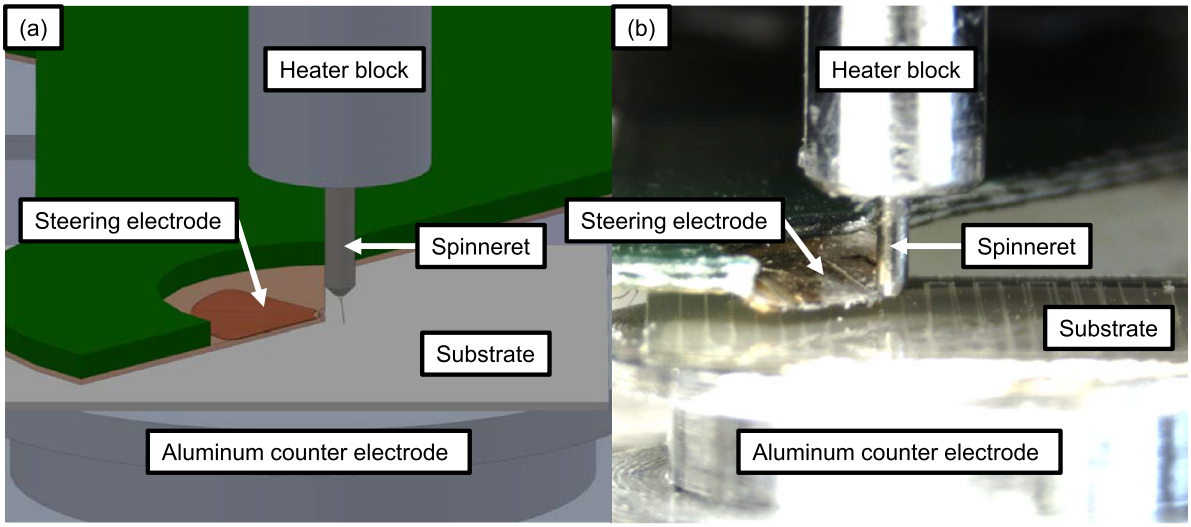

Figure 2. Printing setup with the major components labeled. (a) 3D model, (b) photo of the setup used in the experiments.

inserted into a heating block that surrounded the tip of the syringe. A close-up of the setup can be seen in figure 2. Up to 8 bars of pressure could be applied to the back of the microsyringe via nitrogen gas. The polycaprolactone (PCL) used for printing was purchased from Sigma Aldrich (Mn 45 000, 704 105–100G). A steering electrode was mounted to the side and below the spinneret, perpendicular to the main printing direction. The electrode had earlier been developed in-house and consists of an embedded copper trace on a PCB, the PCB closest to the spinneret is flexible polyimide [28]. This electrode was connected to a high-voltage amplifier (Trek model 610E). The spinneret of the printing head was connected to ground, while the substrate holder was connected to the positive terminal of a high-voltage source (Spezialelektronik iSeg S3CP030 0–3 kV).

The XYZ-stage was controlled via a LabVIEW program developed in-house, this same program was used to toggle the active steering of the PCL jet on or off. The plastic jet was observed using the image of an Imagesource DMK 233UX263 CCD camera connected to a Nikon SMZ745T stereo microscope. A MATLAB-script was used to analyze the image in real-time to determine the position of the plastic jet, and then calculate a voltage through a proportional-integral (PI) loop to apply to the steering electrode to actively steer the plastic jet to the correct position.

To minimize any vibration to the system, the printing setup was placed on an anti-vibrational table (TMC micro-g 63–521), and a fan-less light source was used (Schott KL300 LED). A humidifier (Winix AW600) was placed in the room, and its outlet was directed to blow humid air over the stage. The humidity and temperature were measured using a Fisherbrand Traceable hygrometer.

2.2. Printing parameters

The printing parameters used in this work are mostly based on previous experiments [28], with some minor modifications. The distance between the spinneret and substrate was set to 500 μm, the steering electrode was placed around 100–150 μm above the substrate, and the height for measuring the position of the plastic jet through the CCD video camera feed was 50–70 μm above the substrate. These distances can be seen in figure 3. To ensure that these distances did not vary much while printing, there was a calibration routine for each sample. This routine consisted of measuring the height variations, i.e. orthogonally to the substrate surface, at the outer points of the sample, and then setting the software to correct for a substrate that is not flat with the movement of the stage. The printing speed was set to 2.5 mm s^{-1}. The pressure and voltage were then adjusted to find a point where the diameter of the fiber was roughly 10 μm with minimal trailing of the fiber, while not getting any whipping. Working parameters were found at an applied pressure of 1 bar, printing temperature of 90 °C, and 2.1 kV potential between the spinneret and the substrate. The nominal voltage applied to the steering electrode was 0.9 kV.

2.3. Closed-loop control

The active control of the PCL jet was performed by continuously regulating the potential on the steering electrode between 0 V and 1.85 kV, with a nominal voltage of 0.9 kV. A stereo microscope with a camera was observing the PCL jet. The image was analyzed using a custom MATLAB code [28]. The user selected the area where the script was to look for the jet (orange box in figure 3), and the desired zero-point of the PCL jet (orange dashed line in figure 3). A PI-based control loop calculated the voltage to apply to the electrode based on the distance between the center of the jet and the zero-point. The P- and I-parameters to use in the control loop were found by increasing the parameters until the jet got into self-oscillation, and then backing off until the jet was stable again. In the case of a high P-value, there was a rapid oscillation, and in the case of a high I-value, there was a slower oscillation. The position of the jet and the voltage applied to the electrode was stored in a file to be available for analysis later. The active steering is only in one direction, horizontally

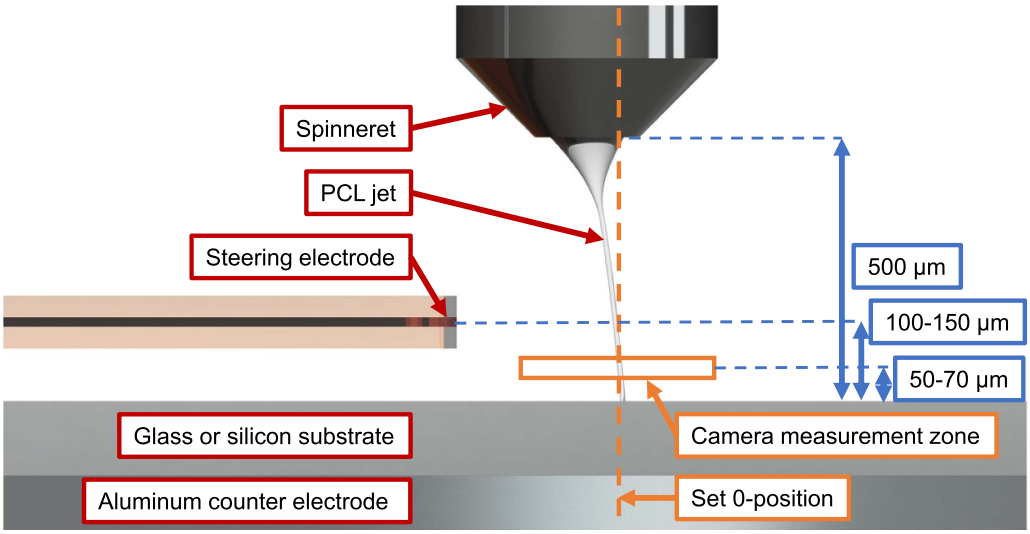

Figure 3. Illustration of the printing setup showing the spinneret, substrate, steering electrode, and PCL jet. Drawn in orange are the camera measurement zone, where the MATLAB-script searches for the PCL jet, and the set 0-position for the script. The important distances in the setup are shown in blue.

in figure 3, as only one electrode and one camera angle were used.

The auxiliary steering electrode [28] was modified for this work by removing some inactive parts of the electrode. Previously, there was material from the flexible PCB on the side opposite the steering electrode (right side in figure 3) which did not have a copper trace. This inactive part was commonly attracting the PCL jet, which caused clogging. The flexible part of the electrode, closest to the spinneret, was also bent down towards the substrate by hand, see figure 2(b). The bent steering electrode enabled control of the PCL jet closer to the substrate surface, figure 3, without any other part of the electrode coming into contact with the substrate surface.

2.4. Printing pattern

The test pattern is presented in figure 4 and consists of 8 mm long parallel printing lines, split into segments of varying distance between the printing lines, ranging from 40 to 75 μm. The printing lines are perpendicular to the control direction of the steering electrode. Half of the segments had a constant voltage on the steering electrode, noted as 'Steering disabled' in figure 4, and the other half used the PI controller with the camera image as input to actively steer the PCL jet to the center, and is noted as 'Active steering enabled' in figure 4. To find out if there was any significant difference in starting with the active steering enabled or disabled, half of the samples were printed with either configuration. In between each segment, there is a separating reference printing line with 250 μm distance to the two segments it separates. These lines were used as reference lines that are assumed to be unaffected by coulombic repulsion and point effect attraction to any fiber printed previously. The segments were printed in two passes, the first of which printed every other line, seen as blue lines in figure 4, and the second pass printed lines between the ones printed in the first pass, the dashed orange lines in figure 4.

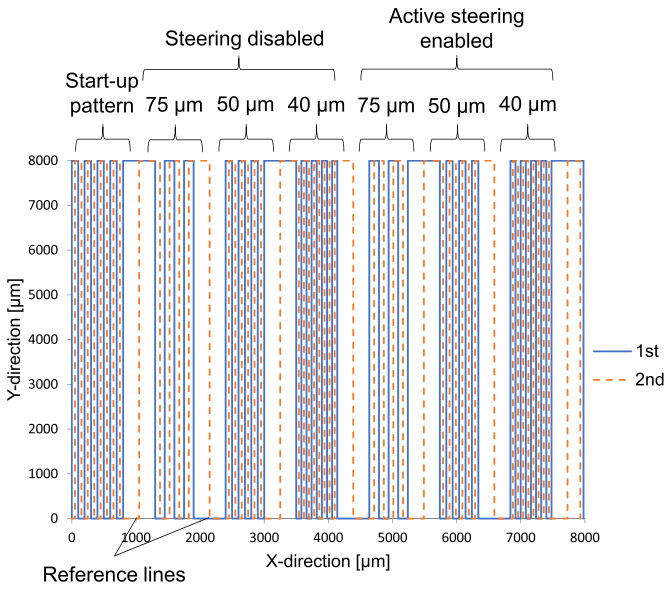

Figure 4. The printing pattern used in the experiments. The 1st and 2nd lines indicate the first and second pass of the printing. Also displayed are various features present in the pattern. Given distances, 40–75 μm, regard the distance between the lines in the pattern after the second pass. For half of the samples, active steering disabled and enabled are switched around, so the active steering is enabled from the start.

This gave more time for charges to disperse, with approximately 170 s between passes, and it made the lines of the second pass go in-between two previous lines. Each print was preceded by a start-up pattern of nine lines, which printed for enough time to stabilize the Taylor cone and fiber thickness. The start-up pattern was also the time where the operator sets the zero-point for the active steering (orange dashed line in figure 3), which is the point the PI algorithm tried to hold.

A separate, modified pattern was repeatedly printed to form 3D-structures. The pattern follows the same as in figure 4, but contains added lines in the *X*-direction spaced out with 200 μm separation. This creates a crossing pattern that can be repeated to create a taller, more complex structure. With each repeated layer, the substrate was lowered 25 μm to compensate for the height of the plastic deposited on the substrate. 2 $\times$ 10 μm is needed to compensate for fiber height at crossing points and an additional 5 μm lowering was used to compensate for uncontrolled factors.

2.5. Software

Different MATLAB-scripts were developed in-house for data acquisition [28] and were slightly modified for this work. One of these scripts extracts the position of deposited PCL fibers from the light optical microscopy (LOM) images taken of the substrates. The PCL fibers were observed as dips in brightness compared to the background. The user set parameters for this script, such as the number of data-points to look for, expected distance between the PCL fibers, calibration of pixels per μm, light intensity cut-off, and so on. Some of these, such as the calibration of pixels per μm, were constant throughout all of the measurements, while others, e.g. the light intensity cut-off, had to be changed occasionally based on the light conditions in the images. The calibration to convert the number of pixels in the LOM images to μm on the substrate was performed by printing 14 lines with 0.5 mm distance separation, half of them with the active steering enabled, and half disabled. The distances measured between the lines were then measured in the number of pixels in the LOM images. The average number of pixels between the fibers was used to calibrate to 500 μm for the rest of the measurements. The number of pixels was measured using the software ImageJ. Some of the LOM images had to be modified, as dirt would show up as dark spots and be mischaracterized by the script to be PCL fibers. The modification consisted of adding a rectangle covering the dirt, with the same color as the lighter gray background. Also, the user has to manually account for any double or triple fibers, by finding them and typing in the coordinates into MATLAB. The manually added lines were drawn out as yellow.

As described in section 2.3 closed-loop control, a MATLAB script was used to determine the position of the PCL jet above the substrate during the printing procedure. The script also logged the positional data found, as well as the calculated voltage to apply. Again, the PCL jet was detected by looking for a dip in the light intensity input into the camera, as the Taylor cone and PCL jet were seen as a dark silhouette on a light background. To dampen the impact of noise, the 2D-image was averaged out to a single row of light intensity points crossing the PCL jet.

2.6. Electric field simulations

To visualize the electric fields and how they are affected by the steering electrode, a simplified 2D model was set up and simulated using COMSOL Multiphysics 5.5. The model uses a grounded truncated rectangle as the spinneret, 500 μm above a glass slide of 140 μm thickness. Below the glass slide, an aluminum rectangle with a potential of 2.0 kV acts as the counter electrode. The steering electrode is emulated as a thin copper rectangle 100 μm above the glass slide, and 200 μm offset from the centerline of the spinneret. The potential of the steering electrode was changed within the range of potentials used in the experiment to see how it affected the electric fields, and thereby the plastic jet.

3. Results and discussion

Figure 5 shows the simulations of the electric fields present with the steering electrode in use. A strong repulsion from the steering electrode can be seen when the applied potential is 0 V. The nominal potential of 900 V gives a slight repulsion, also shown in the illustration in figure 3. In figure 5(c), the steering electrode's potential is simulated at the hard-coded maximum value of the feedback system, 1850 V. The central streamlines are bent towards the steering electrode, but not as sharply as the repulsive bend at 0 V in figure 5(a). Note that the streamlines and the plastic jet are not straight down at 900 V; that potential is still used to give significant control in both directions, being close to the center of the applied voltage range of 0 to 1850 V. There is no need to strive for a perfectly orthogonal central streamline, hence jet direction, but rather to get a sufficiently large and controllable adjustment span around a nominal/middle jet trajectory.

The humidity measured close to the printing setup remained at 60 $\pm$ 5% at 21 °C throughout the experiment. Printing at a significantly lower humidity without the humidifier has typically resulted in unstable printing behavior. Figure 1(a) was an example of printing behavior at low relative humidity.

Figure 6 shows examples of printing behavior and generated lines by the LOM-image data acquisition MATLAB-script. The PCL fibers were printed from the right to the left sides in the images, split up in two passes. The printed fibers furthest to the right in the figure are the reference lines, which are used as 0-position for the distance measurements. The drawn blue lines are the expected positions of the PCL fibers based on the pattern, starting with a 250 μm space between the reference line and the first in the series, and then 40 μm between the rest. The green short lines are the center positions of detected PCL fibers and the yellow short lines are added by the user, where fibers on top of each other, double-stacked fibers, are identified. One measurement is made for each drawn red rectangle, 47 measurements in the vertical direction per PCL fiber. These two examples, figure 6, are representative because they have a standard deviation close to the average deviation of all the samples in the same categories. In the example, and in most samples, when the active steering is disabled and the lines are separated by 50 or 40 μm, double-stacked fibers will be formed due to deflection of the electric field from extruding fibers, the sharp edge effect, and decreased distance between deposited PCL and spinneret, causing an attracting force. There are no double-stacked PCL fibers in the example when the active steering is enabled. The difference between double-stacked and single fibers can be

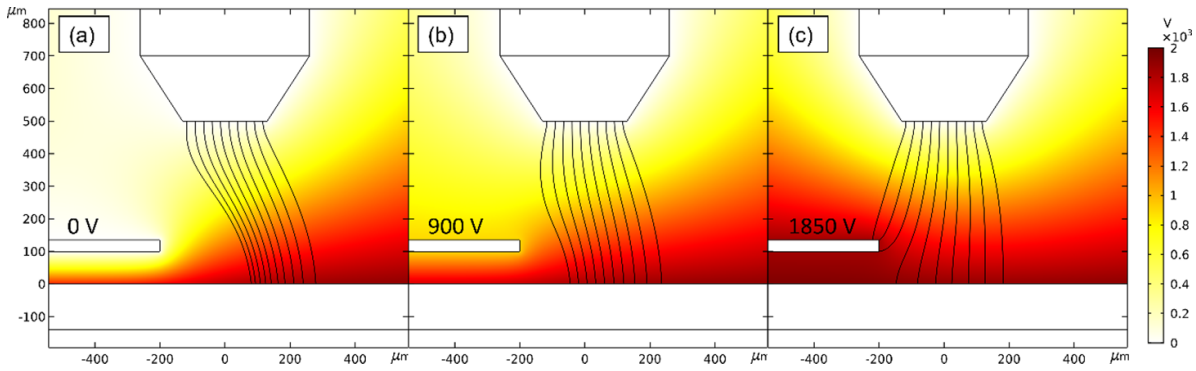

Figure 5. Results of FEM 2D-simulations of a simplified version of the setup used, with the steering electrode being exposed copper. The colored gradient is the electric potential, and the streamlines are the directions of the electric field in the setup. The applied potential on the steering electrode (a) 0 V, (b) 900 V, (c) 1850 V, the spinneret is at ground potential, and the substrate at 2000 V.

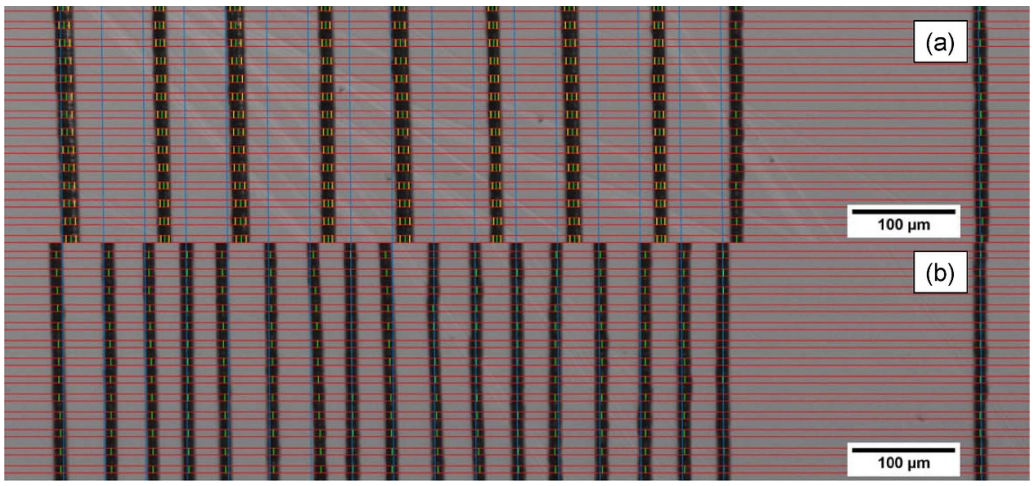

Figure 6. LOM images of samples, where the distance between lines was set to 40 μm, with the printing order going right to left. The lines furthest to the right are reference lines printed 250 μm away from the rest of the pattern. Examples are samples with (a) no active steering, and (b) with steering enabled. Overlaid in red are sections where the custom MATLAB script looks for the PCL fibers, green lines are the centers of detected PCL fibers, yellow lines are where double-stacked PCL fibers were identified and divided into two measurements, and blue lines are the lines where the script expects plastic to be, based on the pattern.

seen in figure 7(a), where the upper structure in the insert is a double-stacked fiber. With the steering electrode enabled, figure 7(b), the fibers are single fibers, but not consistently in the expected position.

Typical data that is acquired from the LOM images is presented in the right column of figure 8. Displayed are bars that indicate the number of points the script found within 1 μm intervals distance from the expected position. A larger amount of counts close to 0 μm indicates a higher degree of positional accuracy. In the left column of figure 8, related positional data from the PCL jet in flight are presented. The data was taken during the printing procedure, using the camera mounted to the stereo microscope. For the substrate data with steering disabled in figure 8, there is a noticeable split of the position, which is due to most fibers being double-stacked fibers, leading to roughly half of the points will be in two separate peaks on either side of the 0 μm point. With the steering electrode enabled, the distribution forms one centered peak. The zero-point of the PCL jet in flight is the value that was set by the operator during the start of the print. If this value was incorrectly chosen, i.e. if it was not to the nominal/middle position of the PCL jet, the mean value of the PCL jet in flight will be offset when the steering is disabled. Similarly, the zero-point of the PCL fiber on the substrate is based on the reference PCL fiber, and if the reference fiber is offset, it will affect the mean value of the test. Therefore, the mean values of the distributions should not be emphasized.

Normal distributions were fitted to all the individual measurements and are shown as red bell curves in figure 8. The 1-σ standard deviations of the distributions are presented in a compiled format in figure 9. Figure 9 shows the combined deviations from six different samples, fiber positions from both the substrate and from the PCL jet in flight, measured 50–70 μm above the substrate through the video camera. Figure 9 also presents data from the different parts of the pattern that have different distances between the printed lines. The results are presented for the steering enabled and disabled side by side. In the segments with 75 μm between the fibers, there is

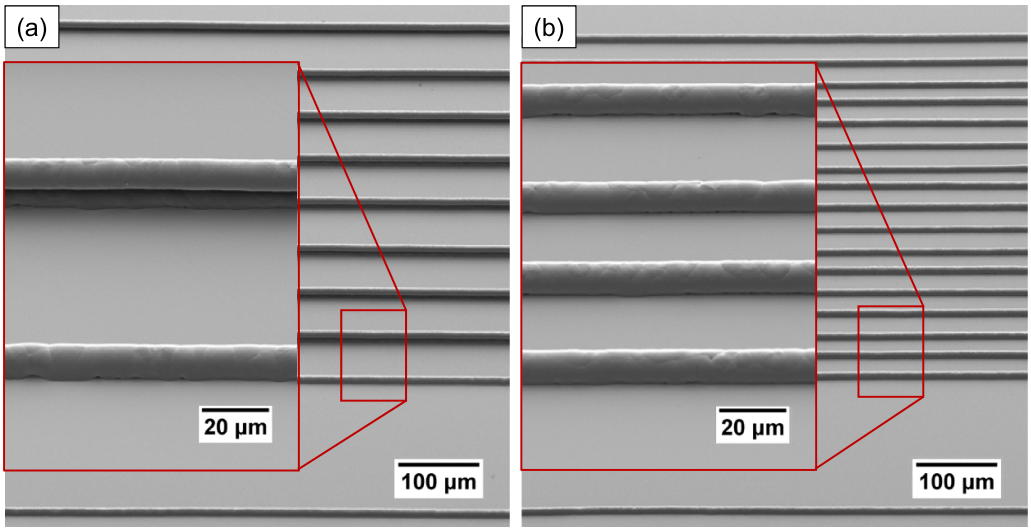

Figure 7. Secondary electron SEM images of the printed structure in figure 6, tilted to approximately 45°, where the distance between lines was set to 40 μm. (a) Pattern printed with no active steering showing double-stacked PCL fibers, (b) pattern printed with active steering showing no stacking of fibers on the substrate.

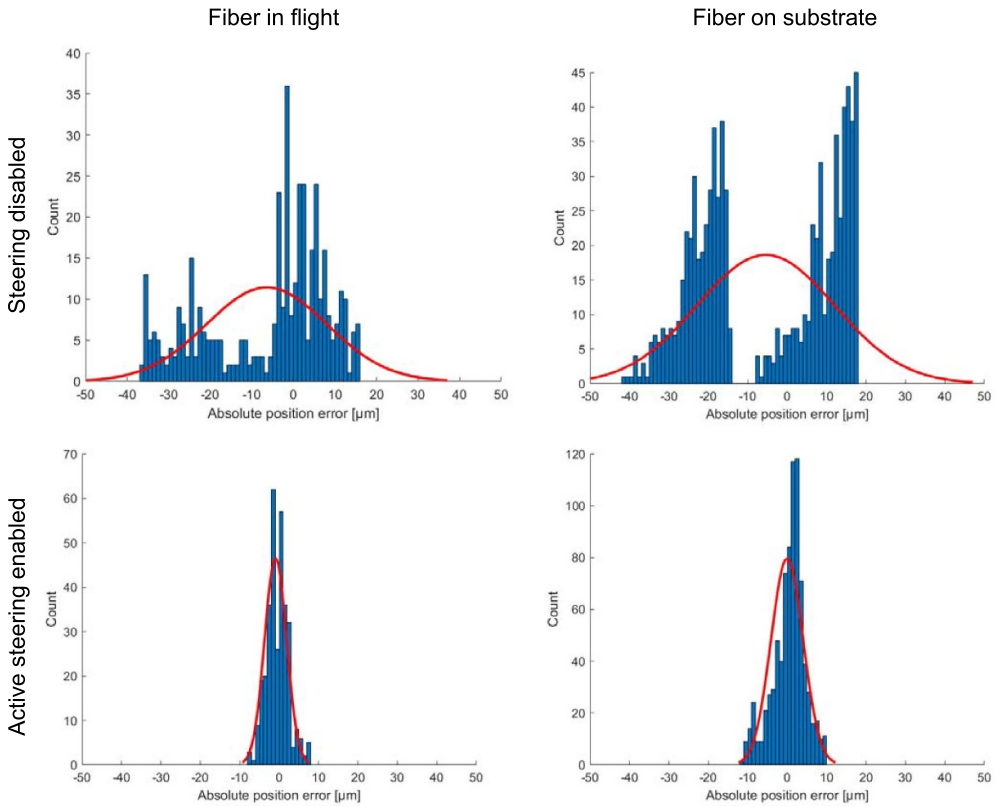

Figure 8. Typical position data from the 40 μm separated pattern of a single sample. The top row presents results from having active steering disabled, and the bottom row with active steering enabled. The left column is taken from the PCL jet in flight through the video camera measurements, and the right column is the positions on the substrate, taken with LOM imaging, see figure 6.

relatively small deviations between PCL jet in flight and fiber on substrate measurements both with and without active steering. This is likely due to a sufficiently large distance between the spinneret and the previously printed charged fibers to avoid disturbances, which also means that the influence of the electric field on the PCL jet was low [5]. The difference having the active steering enabled or disabled was more pronounced with a 50 and 40 μm separation, especially when looking at the results measured above the substrate by the video camera image, from which the MATLAB script controlled the voltage of the steering electrode. When the active steering was enabled, the standard deviations of the PCL jet in flight were in

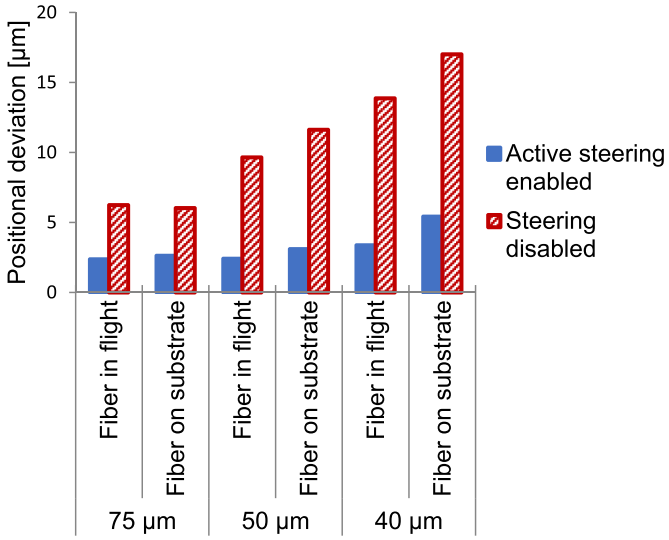

Figure 9. Standard deviation of recorded positions showing the difference between the active steering electrode being enabled or disabled. The position recorded of the PCL jet in flight by the video camera is presented along the positions measured on the substrate by LOM imaging. Different inter-line distances in the pattern are presented separately.

the order of a few micrometers, which was close to the measurement accuracy in the video camera image (about 1 μm). When the distance between the PCL fibers was 40 μm, the standard deviation measured of the PCL jet in flight was lower than the standard deviation of the PCL fibers on the substrate, which agrees well with an expected more precise control at the camera measurement height. As the control loop operated at the height where the PCL jet position was measured, the 50–70 μm above the surface, the fiber placement is expected to degrade somewhat before arriving at the substrate.

We believe that if the in-flight PCL jet position is measured close to the surface, the distance between the PCL fibers could be decreased further without forming double-stacked fibers, possibly allowing for the construction of dense structures with no lateral separation between fibers. Additionally, using two camera angles would allow for the position of the PCL jet to be determined in two dimensions. Using two steering electrodes, the PCL jet could be controlled in both directions in such a setup.

The video camera positional data is considered to be more relevant in this work than the position on the substrate in determining the effects of the steering electrode on the PCL jet. Ideally, the position of the PCL jet would be determined at the surface of the substrate to apply control on that level, but the setup used in this work is currently not capable of doing that reliably. It is reasonably straightforward to detect the PCL jet at a distance 50 μm above the surface with standard image analysis techniques but to detect the PCL jet position when it arrives at the substrate surface demands more advanced image processing algorithms since the image gets more complex in a general case. A method of characterizing a plastic jet in real-time during NFES has previously been developed [29]. The method presented in the article used the Canny edge detector to outline the plastic jet from a video camera. The plastic jet was then traced from the spinneret down to the substrate surface.

While each PCL fiber was 8 mm in length in the pattern, the data was only taken in the approximate center of the fibers to prevent corners from affecting the position of the fibers. An additional reason was to ensure that the measurements were done in the same part of the pattern both on the substrate and in the video camera data.

In figure 10, SEM images of 3D structures printed with and without active control in the indicated direction are shown. The control direction is represented by arrows in figures 10(b) and (d). The fibers that were printed parallel to the control direction, hence those that were not affected by the steering electrode, had a fixed spacing of 200 μm and were used as an aid to reveal printing defects for the controlled fibers, those that were orthogonal to the control directions. Where the perpendicular walls crossed, height was added from fibers deposited in both directions, and therefore the structure got taller in these points than in the walls between the crossings. When the height difference between the crossing points and the center of the walls was large, gaps were formed between fibers in those walls and can be seen in all structures in figure 10. The distances between fibers orthogonal to the control direction in figure 10 are 75 and 50 μm. With 75 μm separation between the lines, the section with the active control, figure 10(b), gave a uniform pattern. The same separation with the active control turned off, figure 10(a), gave uneven heights of the walls due to some double-stacking fibers and varying separation. At the lower separations of 50 μm, further errors can be observed. With the active steering disabled, figure 10(c), almost all lines became double-stacked. With active steering enabled, figure 10(d), some double-stacking is apparent in the last two layers. Smaller separation than 50 μm gave more uneven structures and are not presented here. With this, we can estimate that the minimal separation possible, while active steering is enabled, is reduced to roughly half compared to having steering disabled. As discussed previously, an image analysis algorithm detecting the fiber position where it is placed on the printed structure should allow a further improved interspacing control. The interesting question is if this would allow the fibers to be placed next to each other for a dense 3D structure. An issue regarding the robustness of this NFES-process was more apparent when adding several layers to samples to form 3D structures, as more double-stacked fibers were observed. A problem that persisted throughout this work was that bubbles in the melted PCL disrupted the flow of material through the spinneret occasionally. As the bubble passes through the spinneret, the diameter of the PCL jet will change from the normal diameter of 10 μm, becoming thicker or thinner at times. The thicker fiber was observed to trail more and the thinner fiber can undergo whipping. This occurred seldom and therefore did not significantly affect the results.

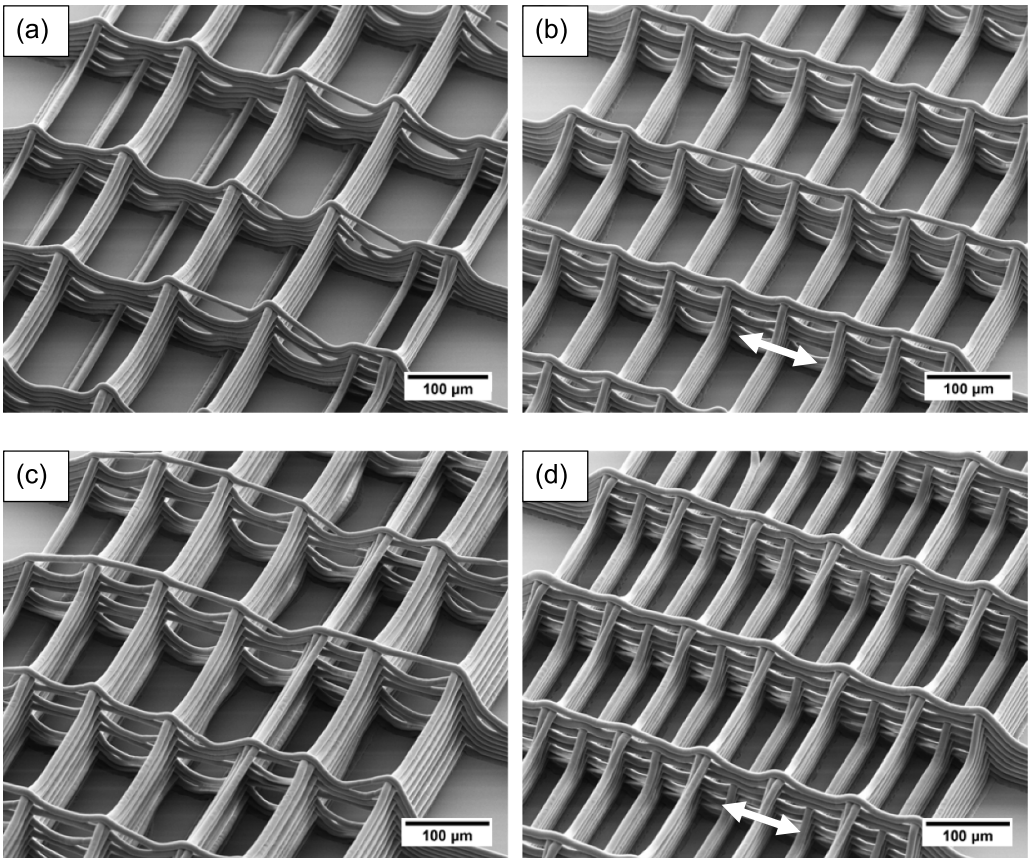

Figure 10. Secondary electron SEM images of printed 3D structures comparing active steering disabled in (a) and (c) to active steering enabled in (b) and (d). The images are tilted to 45°. In (a) and (b), the distance between lines was set to 75 μm, and in (c) and (d), the distance between lines was set to 50 μm. The white arrows in (b) and (d) indicate the direction of control applied from the control loop.

4. Conclusions

The use of an active steering electrode where a camera provides positional feedback of the PCL jet results in a significant increase in the placement accuracy of polymer fibers printed in high density patterns, estimated to roughly double the possible density of structures. The effect is more noticeable on the PCL jet in flight, where the control loop of the fiber placement operates but had an effect on the position further down on the substrate as well. The accuracy of the fiber in flight was controlled to a few micrometers, close to the limit of the measuring system. However, with the setup presented here, it would not be possible to build dense structures of polymer fibers precisely placed in contact with each other laterally, as the positional measurement is too far from the substrate surface. A large improvement is expected to be possible if the camera feedback used the position of the PCL jet just as it reaches the surface of the substrate. This would possibly enable printing of dense structures, but would then require the implementation of more sophisticated image analysis to detect the PCL jet without being disturbed by polymer material already deposited on the substrate.

The control of the plastic jet was only in one direction. To have control in both the x- and y-directions, a setup would require at least one more electrode and an additional camera. This would make it possible to develop the NFES printing technique into a more general additive manufacturing method.

Acknowledgments

We gratefully acknowledge the financial support from the Swedish Research Council [Contract Number 2018-04064].

ORCID iD

Anton Karlsson https://orcid.org/0000-0003-0240-7982

References

[1] Sun D, Chang C, Li S and Lin L 2006 Near-field electrospinning *Nano Lett.* **6** 839–42
[2] Hutmacher D W and Dalton P D 2011 Melt electrospinning *Chem. Asian J.* **6** 44–56
[3] Brown T D, Dalton P D and Hutmacher D W 2011 Direct writing by way of melt electrospinning *Adv. Mater.* **23** 5651–7
[4] Hochleitner G, Jüngst T, Brown T D, Hahn K, Moseke C, Jakob F, Dalton P D and Groll J 2015 Additive manufacturing of scaffolds with sub-micron filaments via melt electrospinning writing *Biofabrication* **7** 035002

[5] Ding H, Cao K, Zhang F, Boettcher W, Chang R C and Fundamental A 2019 Study of charge effects on melt electrowritten polymer fibers *Mater. Des.* **178** 107857
[6] Wei C and Dong J 2013 Direct fabrication of high-resolution three-dimensional polymeric scaffolds using electrohydrodynamic hot jet plotting *J. Micromech. Microeng.* **23** 025017
[7] Luo G, Teh K S, Liu Y, Zang X, Wen Z and Lin L 2015 Direct-write, self-aligned electrospinning on paper for controllable fabrication of three-dimensional structures *ACS Appl. Mater. Interfaces* **7** 27765–70
[8] de Lima. Burgo T A, Rezende C A, Bertazzo S, Galembeck A and Galembeck F 2011 Electric potential decay on polyethylene: role of atmospheric water on electric charge build-up and dissipation *J. Electrost.* **69** 401–9
[9] Bu N, Huang Y, Duan Y, Ding Y and Yin Z 2015 Near-field behavior of electrified jet under moving substrate constrains *AIP Adv.* **5** 017138
[10] Shin D, Kim J and Chang J 2018 Experimental study on jet impact speed in near-field electrospinning for precise patterning of nanofiber *J. Manuf. Process.* **36** 231–7
[11] Jiang J, Wang X, Li W, Liu J, Liu Y and Zheng G 2018 Electrohydrodynamic direct-writing micropatterns with assisted airflow *Micromachines* **9** 456
[12] Zhao Y, Jiang J, Li W, Wang X, Zhang K, Zhu P and Zheng G 2016 Electrospinning jet behaviors under the constraints of a sheath gas *AIP Adv.* **6** 115022
[13] Zheng J, Zhang K, Jiang J, He G, Xu L, Liu Y, Liu J, Wu D and Zheng G 2016 Electrohydrodynamic direct-writing orderly pattern with sheath gas focusing *AIP Adv.* **6** 115304
[14] Deitzel J M, Kleinmeyer J D, Hirvonen J K and Beck Tan N C 2001 Controlled deposition of electrospun poly (ethylene oxide) fibers *Polymer* **42** 8163–70
[15] Bellan L M and Craighead H G 2006 Control of an electrospinning jet using electric focusing and jet-steering fields *J. Vac. Sci. Technol.* B **24** 3179–83
[16] Tse L and Barton K 2014 A field shaping printhead for high-resolution electrohydrodynamic jet printing onto non-conductive and uneven surfaces *Appl. Phys. Lett.* **104** 143510
[17] Vaquette C and Cooper-White J 2012 The use of an electrostatic lens to enhance the efficiency of the electrospinning process *Cell Tissue Res.* **347** 815–26
[18] Han Y and Dong J 2016 Design of integrated ring extractor for high resolution electrohydrodynamic (EHD) 3D printing *Proc. Manuf.* **5** 1031–42
[19] You X, Ye C and Guo P 2017 Electric field manipulation for deposition control in near-field electrospinning *J. Manuf. Process.* **30** 431–8
[20] Lee J, Lee S Y, Jang J, Jeong Y H and Cho D W 2012 Fabrication of patterned nanofibrous mats using direct-write electrospinning *Langmuir* **28** 7267–75
[21] Jeong Y H and Lee J 2016 Fabrication of microfiber patterns with ivy shoot-like geometries using improved electrospinning *Materials* **9** 266
[22] Lee M and Kim H Y 2014 Toward nanoscale three-dimensional printing: nanowalls built of electrospun nanofibers *Langmuir* **30** 1210−4
[23] Grasl C, Arras M M L, Stoiber M, Bergmeister H and and Schima H 2013 Electrodynamic control of the nanofiber alignment during electrospinning *Appl. Phys. Lett.* **102** 053111
[24] Arras M M L, Grasl C, Bergmeister H and Schima H 2012 Electrospinning of aligned fibers with adjustable orientation using auxiliary electrodes *Sci. Technol. Adv. Mater.* **13** 035008
[25] Karatay O, Dogan M, Uyar T, Cokeliler D and Kocum I C 2014 An alternative electrospinning approach with varying electric field for 2-D-aligned nanofibers *IEEE Trans. Nanotechnol.* **13** 101–8
[26] Zhu Z, Chen X, Huang S, Du Z, Zeng J, Liao W, Fang F, Peng D and Wang H 2015 The process of wavy fiber deposition via auxiliary electrodes in near-field electrospinning *Appl. Phys.* A **120** 1435–42
[27] Martinez-Prieto N, Abecassis M, Xu J, Guo P, Cao J and Ehmann K F 2015 Feasibility of fiber-deposition control by secondary electric fields in near-field electrospinning *J. Micro Nano Manuf.* **3** 041005
[28] Bergman H 2019 Increasing the writing resolution for electro-hydrodynamic 3D-printing by active steering of e-jet *MSc Thesis* Uppsala University (available at: http://urn.kb.se/resolve?urn=urn:nbn:se:uu:diva-393068)
[29] Singh R, Zhang X, Chen Y, Zheng J and Qin H 2018 *In-situ* real-time characterization of micro-filaments for electrohydrodynamic ink-jet printing using machine vision *Proc. Manuf.* **17** 45–52